Mid-Holocene variability of the East Asian monsoon based on bulk organic δ^{13}C and C/N records from the Pearl River estuary, southern China

Fengling Yu,[1,2] Yongqiang Zong,[3] Jeremy M Lloyd,[1] Melanie J Leng,[4] Adam D Switzer,[2] Wyss W-S Yim[3,5] and Guangqing Huang[6]

Abstract
Understanding the mid-Holocene dynamics of the East Asian monsoon (EAM) is integral to improving models of the Holocene development of the global climate system. Here we reconstruct the mid-Holocene EAM history from the Pearl River estuary, southern China, using bulk organic carbon isotopes (δ^{13}C), total carbon to total nitrogen (C/N) ratios and total organic carbon (TOC) concentration. Sedimentary δ^{13}C, C/N and TOC are potentially good indicators of changes in monsoonal precipitation strength. Sediments buried during a period of high precipitation exhibit a high proportion of terrigenous material, and have low δ^{13}C and high C/N, and vice versa during a period of low precipitation. Results suggest a general decreasing trend in monsoonal precipitation from 6650 to 2150 cal. yr BP because of the weakening Northern Hemisphere insolation most likely related to the current precession circle. Superimposed on this trend are apparent dry–wet oscillations at centennial to millennial timescales most likely in response to solar activity. Mismatches between our δ^{13}C record and results from the Dongge Cave in southern China at millennial timescales may indicate that the δ^{13}C from the Pearl River estuary reveals changes in precipitation over a broader area than the δ^{18}O from Dongge Cave.

Keywords
bulk organic δ^{13}C, C/N, China, East Asian monsoon history, Holocene, Pearl River estuary, solar forcing

Introduction

The East Asian monsoon (EAM) forms as a result of unequal heating of the Asian landmass and the Pacific and Indian Oceans (Figure 1a) and subsequent energy re-distribution. At the present day the EAM plays a significant role in the global and regional hydrological and energy cycles (Webster et al., 1998). It is suggested that fluctuations during the Holocene exerted a major influence on human societies (Mischke and Zhang, 2010; Shi et al. 1994). For example, during the stable warm and wet phase from 7200 to 6000 cal. yr BP, the Neolithic Yangshao Culture in the Yellow River catchment and the Majiabang Culture in the lower Yangtze plain, reached their climax (Shi et al., 1994). A sudden dry and cold event around 4000 cal. yr BP recorded in the Dunde ice core, Northwest China (Thompson et al., 1989, 1993), is suggested to be responsible for the end of the Longshan and Liangzhu Cultures in East China (Shi et al., 1994). Nearly two-thirds of the world's population live in areas influenced by the EAM. A better understanding of the past variability of the EAM and the associated links with human cultures is, therefore, crucial to improve our understanding of potential implications of future changes in monsoon climate.

The history of the EAM during the Holocene can be regarded as an alternation between dominance of a cold-dry winter monsoon and a warm-wet summer monsoon (An, 2000). After the Younger Dryas (11 200–10 000 cal. yr BP), a cold period which might have included some dry/wet oscillations (Xiao et al., 1998), the EAM switched to relatively warm and wet conditions (the Holocene). Based on evidence from ice cores (e.g. Thompson et al., 1989, 1993), lake water levels (e.g. Li et al., 1990; Wang

and Fen, 1991), as well as archaeological records (e.g. Zhou et al., 1991), Shi et al. (1994) suggested that Holocene Megathermal phases mainly occurred during 8500–3000 cal. yr BP. They divided the Holocene EAM into several phases: 8500–7200 cal. yr BP characterised by unstable temperature fluctuations with an increase in precipitation; 7200–6000 cal. yr BP was a stable, warm and wet phase when the monsoon rainfall occurred almost throughout China; 6000–5000 cal. yr BP was characterized by strong climatic fluctuations and adverse climatic conditions; after 5000 cal. yr BP the climate became warm and stable – suitable for cultural development in China. Around 4000 cal. yr BP, the climate deteriorated and catastrophic floods occurred in East China; from 4000 to 3000 cal. yr BP, the climate was warm and humid. Based on geological data and numerical modelling, An et al. (2000) suggested that the front of the EAM retreated from

[1]University of Durham, UK
[2]Nanyang Technological University, Singapore
[3]The University of Hong Kong, China
[4]British Geological Survey, UK
[5]City University of Hong Kong, China
[6]Guangzhou Institute of Geography, China

Corresponding author:
Fengling Yu, Department of Geography, University of Durham, South Road, Durham DH1 3LE, UK.
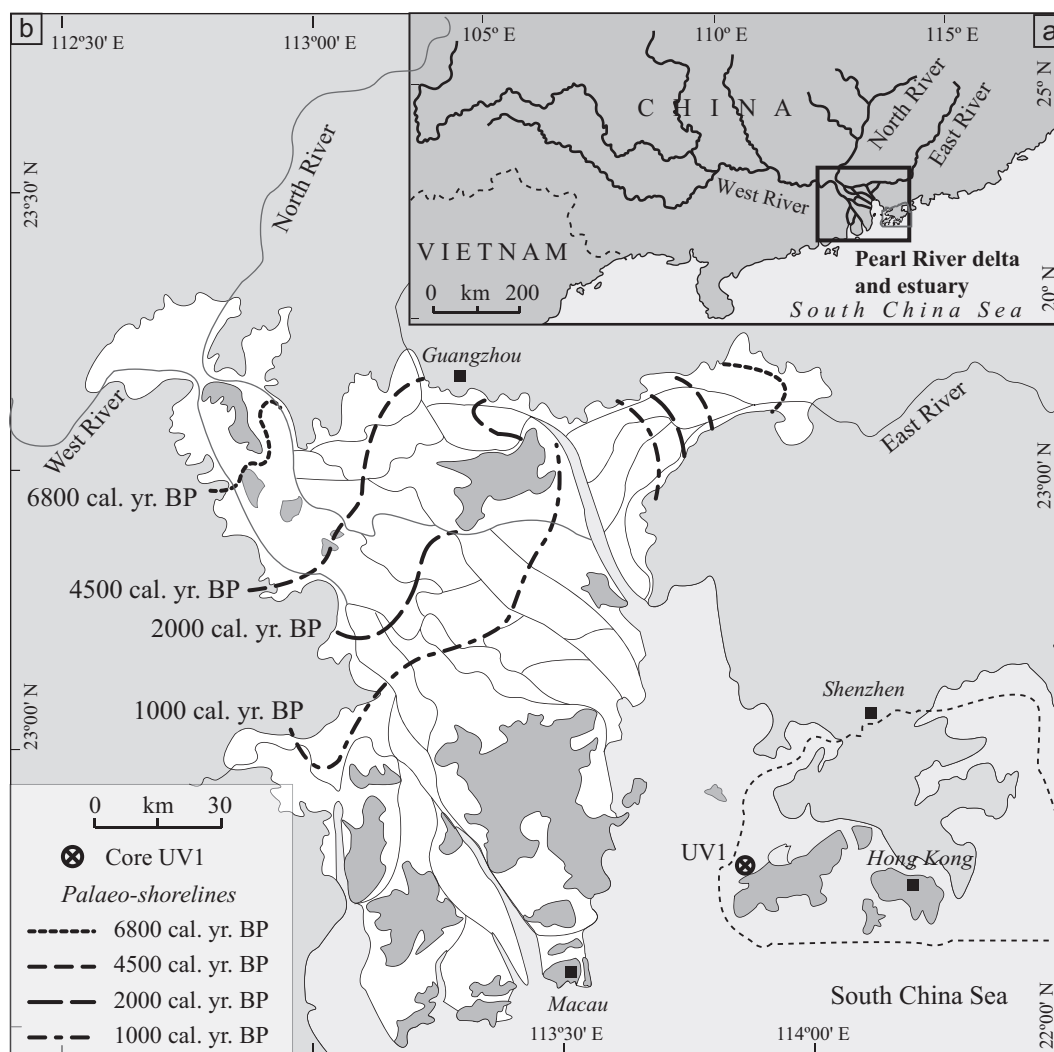Email: fengling.yu@ntu.edu.sg

Figure 1. Study area. (a) Location of Pearl River estuary, East Asia; (b) locations for core UV1 (this study) and palaeoshorelines (Zong et al., 2009a)

north to south China during the Holocene. This resulted in the Holocene Optimum, a period of maximum precipitation, occurring earlier in the north and northeast of China and later in the south and southeast. The hydrological and thermal dynamics of the EAM system are perturbed by external and internal factors at a range of timescales. These factors range from solar forcing at millennial timescales, high latitude cooling events at centennial timescales, to low latitude El Niño events at decadal timescales (An et al., 2000).

Variability of the Holocene EAM has been reported from a range of archives, including natural records, such as loess (e.g. Porter and An, 2005), tree rings (e.g. Wu, 1992; Wu et al., 1988), ice cores (e.g. Thompson et al., 1989), and stalagmites (e.g. Wang et al., 2005), as well as historical archives (Shi et al., 1994). Each of these has specific advantages and disadvantages. Loess deposits from the Loess Plateau, central China, are good archives for investigating the EAM over timescales of millions of years. However, it is hard to undertake high-resolution studies based on these records because of the low sedimentation rates. Ice cores and deep-ocean deposits also suffer from a similar problem of low resolution. Stalagmites provide high-resolution studies; however, the $\delta^{18}O$ signature can be influenced by both temperature and precipitation, which are also subject to local scale variability. Historical records can provide valuable information, but can be difficult to interpret and are spatially and temporally fragmented.

This study reconstructs the EAM during the mid Holocene from a estuarine core (core UV1) collected from Pearl River estuary (Figure 1b). Previous studies in the Pearl River estuary have shown that changes in the organic carbon isotopic signature of estuarine sediments can be used as an indicator for changes in the freshwater discharge induced by the monsoonal precipitation (Yu et al., 2010; Zong et al., 2006).

Over centennial and millennial timescales the sources of estuarine sediments (Figure 2) are influenced by relative shoreline movements, sea-level changes, and monsoonal climate change. Zong (2004) re-examined the Holocene sea-level history for the low latitude part of the China coast by re-assessing all the sea-level data available from the east to south coasts. The sea-level curve from west Guangdong and Hainan, a geologically stable region, shows that the relative sea level reached the present-day height by 6200 cal. yr BP and since then has been relatively stable (Zong, 2004). The time of maximum emergence of the sea-level highstand occurs earlier at tidal river sites than at coastal sites (Zong, 2004). In the Pearl River Delta, the maximum emergence of the highstand was around 7000 cal. yr BP (Li et al., 1990; Zong, 2004).

As the sea level in this area has been relatively stable since the mid Holocene, monsoonal climate is one of the most important controlling factors for the sediment flux into the estuary (Li et al., 1990; Wang et al., 2005; Zong et al., 2006). For example, Zhang et al. (2008) suggested a positive linear correlation between
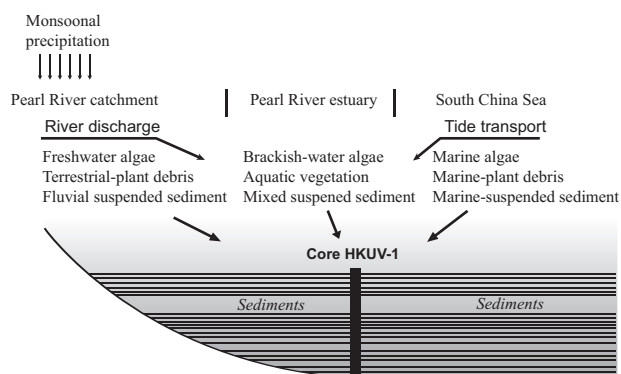
Figure 2. Sediment input into the Pearl River estuary from three main sources including terrestrial, brackish-water and marine areas (adapted from Zong et al., 2006)

cumulative freshwater discharge and cumulative sediment flux in the Pearl River. As outlined by Zong et al. (2006) the Pearl River estuary receives sediments from three main sources: river, marine and in situ brackish-water derived material (Figures 1b, 2); the proportion of these three main sources of organic matter to the estuarine sediment is controlled by the strength of the river discharge due to monsoonal precipitation. Therefore, during a period of strong summer monsoon, increased precipitation levels will generate a large volume of freshwater discharge into the estuary, along with high sediment flux. It follows that estuarine sediments preserved during periods of strong summer monsoon will have a higher proportion of terrigenous sediments compared with periods of stronger winter monsoon (lower precipitation, lower freshwater flux, hence lower proportion of terrigenous sediments relative to marine/brackish sediments). Thus, the monsoon-induced freshwater discharge can be reconstructed by examining changes in the relative dominance of organic matter from the three sources identified above preserved in the Pearl River estuary (Yang et al., 2011; Yu et al., 2010; Zong et al., 2006).

This study applies this methodology to reconstruct the EAM during the mid Holocene at decadal resolution, employing bulk organic carbon isotopes ($\delta^{13}C$) and total carbon to total nitrogen (C/N) ratios, to help understand possible driving mechanisms behind monsoon variability. Application of $\delta^{13}C$ and C/N analyses of sedimentary organic matter for reconstructing palaeoenvironmental changes have been carried out in a range of environments (Lamb et al., 2006), including lagoons (Müller and Mathesius, 1999; Yamamuro, 2000), isolation basins (Chivas et al., 2001; Mackie et al., 2007; Westman and Hedenström, 2002), fjords (Bird et al., 1991; St-Onge and Hillaire-Marcel, 2001; Smittenberg et al., 2004), as well as estuaries (Malamud-Roam et al., 2006; Middelburg et al., 1997; Wilson et al., 2005; Zong et al., 2006). The advantage of $\delta^{13}C$ and C/N analysis is that it can be performed on most sediment, as only a small amount of organic carbon (micrograms to milligrams) is required for analysis. Organic $\delta^{13}C$ and C/N ratios can be measured rapidly and analyses are relatively inexpensive, leading to high-resolution studies (Lamb et al., 2007). To explore driving mechanisms for oscillations of the EAM at millennial to centennial timescales, general trends of $\delta^{13}C$ and other proxies were removed.

Study area

The Pearl River catchment, located between 21°20′–23°30′N and 112°40′–114°50′E (Figure 1a), formed as a result of the uplift of the Tibetan Plateau during the Tertiary and Quaternary periods (Aitchison et al., 2007). Before the late Quaternary, sediment from the river system bypassed the current deltaic basin and was

deposited on the continental slope and shelf (Zong et al., 2009a). Only since the Late Pleistocene has the deltaic basin started to receive sediments from the river system (Huang et al., 1982; Xu et al., 1985). The lower fluvial/deltaic plains of Guangdong and Guangxi provinces have been gradually infilled during the late Quaternary with progradation of the delta front since 6800 cal. BP (Zong et al., 2009a; Figure 1b).

The Pearl River catchment lies in the transitional area between the tropical and subtropical climate zones. The West River, 2214 km in length with a catchment area of 425 700 km², contributes the majority of both water and sediment flux reaching the Pearl River Estuary (Kot and Hu, 1995; Zhang et al., 2008). Under strong influence of the monsoon climate, freshwater discharge and sediment flux show great seasonal variability due to seasonal changes in monsoonal precipitation. The mean annual precipitation of the catchment is 1200–2000 mm, which mainly occurs during the wet season lasting from April to September. Annual discharge of the whole Pearl River system is 330×10^9 m³ (Hu et al., 2006), and the annual sediment load is 89×10^9 kg (Zhang et al., 2008). Statistics since 2002 show that more than 86.9% of the annual suspended sediment is discharged during the wet season and 67.6−83.5% of annual water flux occurs in this season (Shen and Wang, 2009). Seasonal changes in monsoonal precipitation also results in changes in salinity within the estuary. For example, in summer (June–August), high precipitation generates strong freshwater flux into the estuary, resulting in a low-salinity estuarine environment, with water salinity lower than 1 PSU at the river mouth. Saline water intrudes much further upstream in winter (December–February) than in summer because of a significant reduction in freshwater flux (Yu et al., 2010; Zong et al., 2010a). In addition to the seasonal salinity variability, within the estuary there is a northwest–southeast isohaline system, due to decreasing freshwater influence seawards (Yu et al., 2010) and the strong tidal currents in the eastern part of the estuary (Zong et al., 2010a).

Material and methods

Vibracore UV1 was collected from 22°17′10″N, 113°51′49″E (Figure 1b) from a water depth of 8.6 m. The top 10 m of sediment spanning the last *c*. 6500 years was used for this study. The top 0.35 m of the core was washed away during the coring process and sediments from 6.00–6.25 m were missing because of gaps in the sampling tube. The core was sampled at 2 cm intervals for $\delta^{13}C$, C/N and TOC, producing a total of 501 samples.

The chronology for UV1 used here is that of Zong et al. (2010b) and is based on seven radiocarbon dates which are mostly from benthic foraminifera samples collected from various depths (Table 1). There is a small age reversal between GZ2213 at 2.6 m and SUERC-9602 at 1.9 m, the reason for this age reversal is not clear. The sedimentation environment was stable because particle size analysis shows no major change in sand, silt or clay fractions (Zong et al., 2010c), and there is no bioclastic storm bed found in this sediment section (e.g. Huang and Yim, 2001). The only thin sandy layer found in the core is located at 1.0 m (Zong et al., 2010c). Diatom assemblages from the section containing the age inversion show no significant change either (Zong et al., 2010b). All other dates lie in stratigraphic order producing a relatively robust age model (Figure 3; Zong et al., 2010b). Accordingly, these dates suggest a period of steady sedimentation from *c*. 6650 cal. yr BP at 10 m depth to *c*. 3300 cal. yr BP at 2.6 m. The average sedimentation rate in this period is *c*. 0.22 mm/yr. The top 2 m section of the core was deposited in the last 3300 years, with a reduced sedimentation rate of *c*. 0.08 mm/yr (Figure 3).

Table 1. Radiocarbon dates from Core UV1

Depth (m)	Material dated	Conventional age (yr BP)	Method	95% HDR (cal. yr BP)	50% HDR (cal. yr BP)	%C (by weight)	δ^{13}C (‰, VPDB) ± 0.1	Laboratory code
0.5	Shell	Modern						GZ2211
1.3	Foraminifera	2254 ± 30	AMS ^{14}C	2337–2162	2233			GZ2212
1.9	Foraminifera	3019 ± 35	AMS ^{14}C	3333–3087	3232	9.8	−3.1	SUERC-9602
2.6	Foraminifera	2974 ± 33	AMS ^{14}C	3292–3025	3157			GZ2213
4.5	Foraminifera	3963 ± 35	AMS ^{14}C	4516–4299	4434	8.8	−4	SUERC-9605
7.5	Foraminifera	4847 ± 35	AMS ^{14}C	5647–5486	5593	9.7	−4.1	SUERC-9606
9.5	Foraminifera	5633 ± 36	AMS ^{14}C	6486–6320	6413	9	−2.6	SUERC-9607
12.5[a]	Shell	37 900 ± 320	AMS ^{14}C	41 220–40 900	41 600		−1.4	OS-51226

Radiocarbon dates are calibrated using Calcuve Intcal 09, 95% and 50% HDR ages are estimated using Bchron (Parnell et al., 2008), HDR, highest posterior density region; [a]dates are cited from Zong et al. (2009b), where calibrated ages are expressed at ±2σ level.
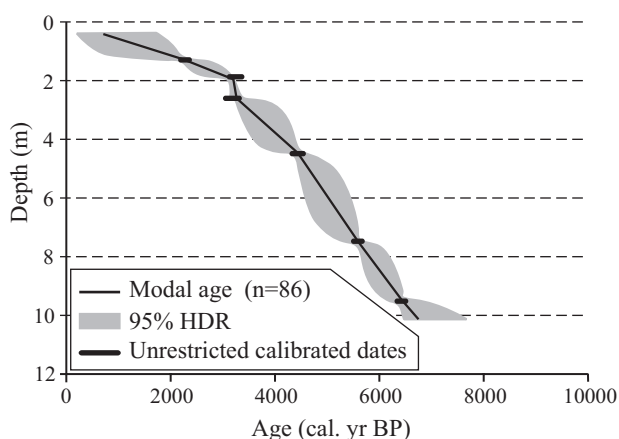

Figure 3. Age model for Core UV1 (modified from Zong et al., 2010b). The age model is established via Bchron using the method suggested by Heegaard et al. (2005) and Parnell et al. (2008). The 95% highest posterior density ranges (HDR) indicate the uncertainty of the ages assigned to each sample between the dated depths, together with the mean modelled age for each sample. In the graph, the number of samples involved in the calibration is shown as *n*, and the modelled age curve is established based on the 50% chronology

Sediment samples for δ^{13}C and C/N analyses were prepared using 100 ml 5% HCl to remove carbonates. They were then washed three times with deionised water using the fibreglass filter paper (Fisher Brand 200), before being dried at 50°C overnight, homogenised in a pestle and mortar, and weighed (25–50 mg) for δ^{13}C and C/N analysis. Carbon isotopes and C/N analyses were performed by combustion in a Carlo Erba NA1500 (Series 1) online to a VG Triple Trap and Optima dual-inlet mass spectrometer, with δ^{13}C calculated to the VPDB scale using a within-run laboratory standards (BROC) calibrated against NBS-19 and NBS-22. Replicate analysis of well-mixed samples indicated a precision of ±<0.1‰ (1SD). C/N was determined by reference to an Acetanilide standard. Replicate analysis of well-mixed samples indicated a precision of ±<0.1%. The isotopic ratios are expressed as δ^{13}C, in units of per mil (‰). The C/N is given using weight ratio of total organic carbon (%TOC) to total nitrogen (%TN). Where duplicate analyses was carried out, the data presented are the average value (SC typically <0.1‰).

For particle size analysis, sediment (0.2−4 g) was soaked in 5% Calgon solution overnight before analysis to allow disaggregation of the sediment. An ultrasonic treatment was applied when the sample did not completely disaggregate. Samples were then stirred before being introduced to the laser granular meter (Coulter LS 13200) for the analysis of fractions of sand, clay and silt. Results of particle size analysis are presented in the format of 'average value ± standard deviation (SD)'.

Exponential smoothing of δ^{13}C and C/N data were performed using the SPSS for Windows program. This method was chosen over other methods such as moving average, because it does not result in data loss, and it catches the general trend of the data series. To compare periodicity between δ^{13}C and other proxies, the new δ^{13}C data presented here was de-trended along with the previously published ^{10}Be (Finkel and Nishiizumi, 1997) and Hematite-strained glass data (HSG, Bond et al., 2001). Spectral analysis on δ^{13}C and ^{10}Be and de-trending of data were carried out using the PAST program (Hammer et al., 2001).

Results

The δ^{13}C, C/N and TOC data are presented in Figure 4. There is a clear change in sedimentation at 10.07 m marking the boundary between Holocene sedimentation above and pre-Holocene sedimentation below (poorly sorted firm clay through to gravel sediments below, soft silt and clay above). This is supported by the radiocarbon date of 33 500 ± 360 cal. yr BP at 12.5 m (Zong et al., 2009b). The age of the base of the Holocene section is estimated at 6650 cal. yr BP based on the age model developed by Zong et al. (2010b) (Figure 3). One of the possible reasons for the absence of early-Holocene deposition is that the core site was subaerially exposed at this time, when the sea level was low (Zong, 2004; Zong et al., 2009a), and sediment only starts accumulating when the sea level stabilized around 7000 cal. yr BP.

The Holocene section of the core is split into two zones based on the lithology, grain size and δ^{13}C values. Zone 1 from 10.07 to 1.30 m is composed of dark greenish grey silt and clay (63.6±5.2% silt and 24.9±3.9% clay; Table 2). Zone 2 from 1.30 to 0.35 m is composed of yellowish silt and clay with a higher proportion of sand (17.0±12.1%; Table 2), mixed with large amounts of shell fragments. There are clear changes in δ^{13}C, TOC and C/N values between Zones 1 and 2 (Figure 4); the average δ^{13}C value for Zone 1 is −25.2±0.3‰, compared with −23.1±2.0‰ for Zone 2 (Figure 4). The radiocarbon date from 0.52 m produced a modern age (108 cal. yr BP), while the date from 1.33 m (immediately below the boundary between Zones 1 and 2) provided an age of 2337–2162 cal. yr BP. Based on the chronology and clear change in character of the sediments, the change from Zone 1 to Zone 2 most likely relates to enhanced human activity in this area as discussed by Zong et al. (2010c). In this paper we concentrate on the mid-Holocene section preserved in Zone 1.

Sediment from Zone 1 is mainly composed of silt (average 63.5 ± 5.2%) and clay (average 24.9 ± 3.9%), while sand concentrations average 11.4 ± 6.6% (Figure 5; Table 2). The proportion of sand and silt are negatively correlated through the core. Clay
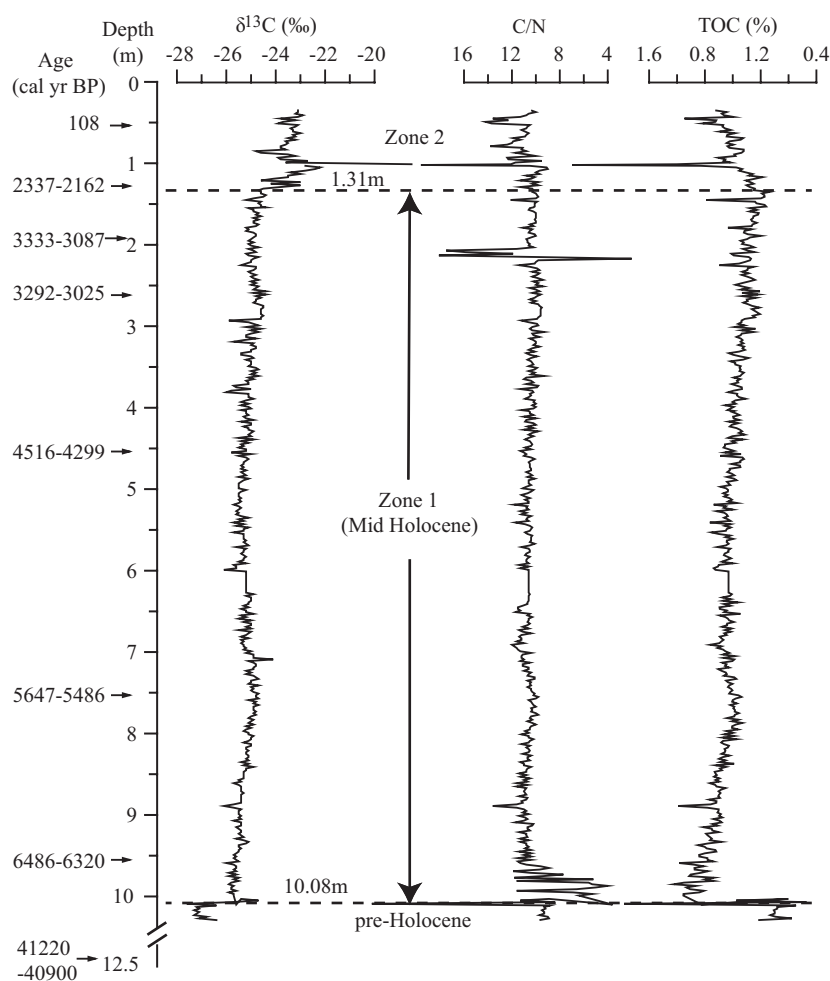
Figure 4. Results of δ¹³C, C/N and TOC for core UV1 (10.29–0.35m)

Table 2. Measurements of Zone 1 and Zone 2 of Core UV1

Depth (m)	Age (cal. yr BP)	δ¹³C (‰)	TOC (%)	C/N	Sand (%)	Clay (%)	Silt (%)
0.35–1.29	1364–1990	−23.1 ± 2.0	0.1 ± 0.0	11.3 ± 1.7	17.0 ± 12.1	22.2 ± 4.4	60.8 ± 10.8
1.31–10.07	2003–6395	−25.2 ± 0.3	0.1 ± 0.0	10.5 ± 1.2	11.4 ± 6.6	24.9 ± 3.9	63.6 ± 5.2

Values are presented as 'average values± the standard deviation'.

concentration gradually decreases from approximately 30.0% at the base to 20.0% at the top of the core.

The δ¹³C values of Zone 1 show a general increasing trend from the base to the top of the zone (Figure 5). Superimposed on this increasing trend, the δ¹³C values fluctuate between −26.4‰ and −24.1‰, the average value (−25.2‰) for Zone 1 is shown by the dashed line (Figure 5). Exponential smoothing of the δ¹³C data suggests two oscillations are recorded in this section. The first complete oscillation starts from the base of this section, *c*. 6650 cal. yr BP to *c*. 4600 cal. yr BP. The second oscillation runs from *c*. 4600 to *c*. 2100 cal. yr BP, although the last part of this oscillation is not so clearly defined and may be incomplete (Figure 5). The mean C/N ratio in Zone 1 is 10.5 (dashed line, Figure 5). C/N ratios in Zone 1 show a general decreasing trend, except for very low C/N ratios (4.0−9.0) from 6650 to 6480 cal. yr BP (Figure 5). TOC records of UV1 show a general decreasing trend from 1.4% to 0.8% throughout Zone 1 with the average value of 1.01% (Figure 5). The exponential-smoothed TOC record shows a relatively close correlation with the δ¹³C values (Figure 5).

Discussion

An East Asian monsoon history during the mid Holocene

The δ¹³C and C/N signature preserved in core UV1 outlined above can be used to infer changes in the sediment sources during the mid Holocene. Changes in sediment source can then be used to indicate changes in EAM precipitation-induced freshwater flux.

General weakening EAM during the mid Holocene. Increasing δ¹³C, decreasing C/N ratios and decreasing TOC found in sediments spanning the period 6650−2150 cal. yr BP indicate a long-term trend of weakening precipitation-induced freshwater discharge linked to a weakening summer monsoon (Figure 5). This trend is highlighted in Figure 6a by higher than average δ¹³C values (−25.2‰) from 4350 to 2150 cal. yr BP and generally lower than −25.2‰ from 6650 to 4350 cal. yr BP. Possible forcing mechanisms that could influence the proportion of sediments from different sources in UV1 during this time period are sea-level change,
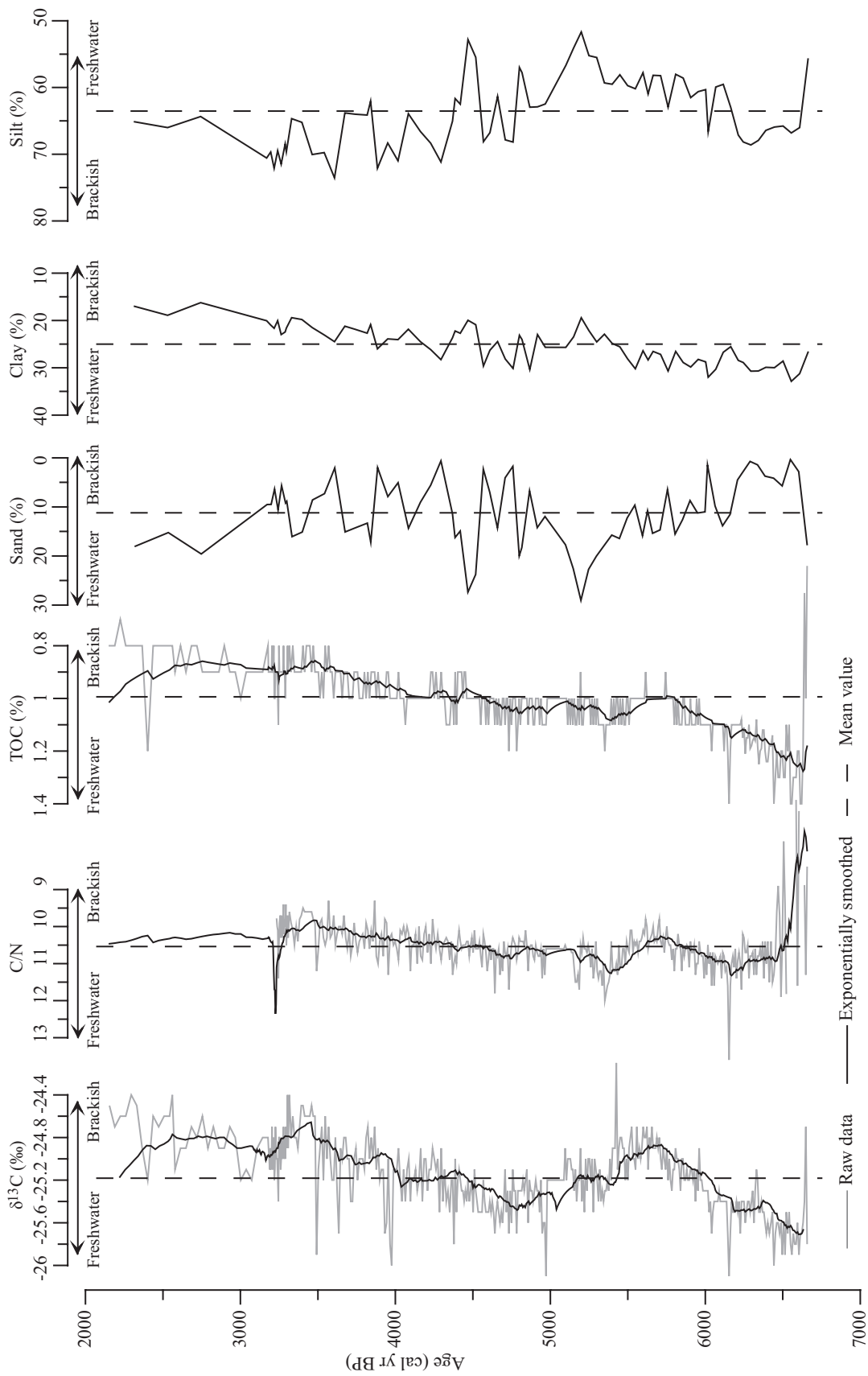
Figure 5. Results of δ^{13}C, C/N, TOC and particle size during the mid Holocene (10.07–1.31 m of core UVI, ranging from 6650 to 2150 cal. yr BP) plotted against calibrated ages at 95% HDR
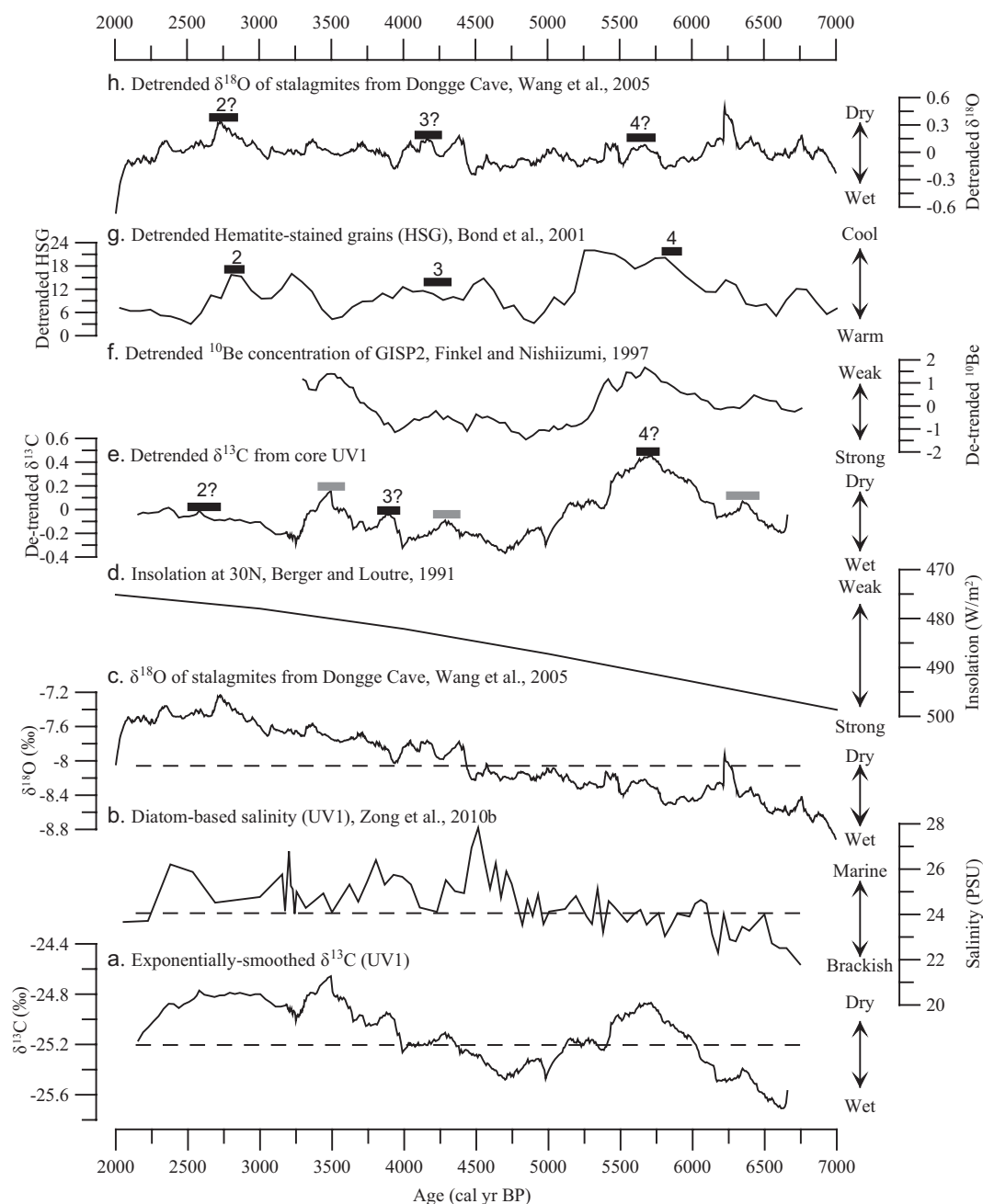
Figure 6. Comparison between $\delta^{13}C$ of UV1 and other records. (a) Exponentially smoothed $\delta^{13}C$ from 6650 to 2150 cal. yr BP (this study); (b) palaeo-salinity based on diatom-salinity transfer function from core UV1 by Zong et al. (2010b); (c) $\delta^{18}O$ of stalagmite from Dongge Cave, southern China (Wang et al., 2005). In (a), (b) and (c), dashlines show the mean value of each proxy. (d) Insolation changes at 30°N (Berger and Loutre, 1991); (e) detrended $\delta^{13}C$ from core UV1 (this study); (f) detrended concentration of ^{10}Be of GISP2 ice core (Alley et al., 1995; Davis et al., 1990; Finkel and Nishiizumi, 1997), where higher ^{10}Be concentration is responding to stronger solar activity; (g) detrended hematite-stained grains (HGS) of Core MC52 and VM29-191 (Bond et al., 2001), with IRD events 2, 3 and 4 (Bond et al., 1997) marked by black bars; (h) detrended $\delta^{18}O$ of stalagmite from Dongge Cave, southern China (Wang et al., 2005). In (e) and (h), black bars show the possible position of IRD events 2, 3, and 4. In (e), grey bars are dry events observed in this study. Detrending of these data was taken using the PAST programme (Hammer et al., 2001)

delta progradation and freshwater flux. Sea level reached its present-day level around 6800 cal. yr BP and has been relatively stable since then (Zong, 2004). Thus, the influence of sea-level changes on the $\delta^{13}C$ signal is assumed to be relatively minor. As a consequence of the stable sea level, the deltaic shoreline advanced slowly seawards between 6800 and 2000 cal. yr BP (Figure 1b, Zong et al., 2009a). Delta progradation during the mid Holocene has led to core UV1 being more proximal to terrestrial source areas through time (Figure 1b). Based on this we would expect larger amounts of terrestrial sediment to be delivered to the core site through time. However, the general increase in bulk organic carbon $\delta^{13}C$ values

recorded in UV1 during the mid Holocene indicates a decreasing proportion of terrestrial organic matter (Figure 6a). Terrestrial/freshwater-sourced organic material has an average $\delta^{13}C$ value of −25.0‰, compared with marine-sourced organic material with an average of −21.0‰ (Hu et al., 2006; Yu et al., 2010; Zong et al., 2006). This suggests that a decrease in terrestrial material input due to lower freshwater flux is far greater than an assumed increase in terrestrial material input expected because of increased proximity associated with delta front advance. This, therefore, suggests that the actual reduction in terrestrial material input (hence freshwater flux) is in fact even more significant.
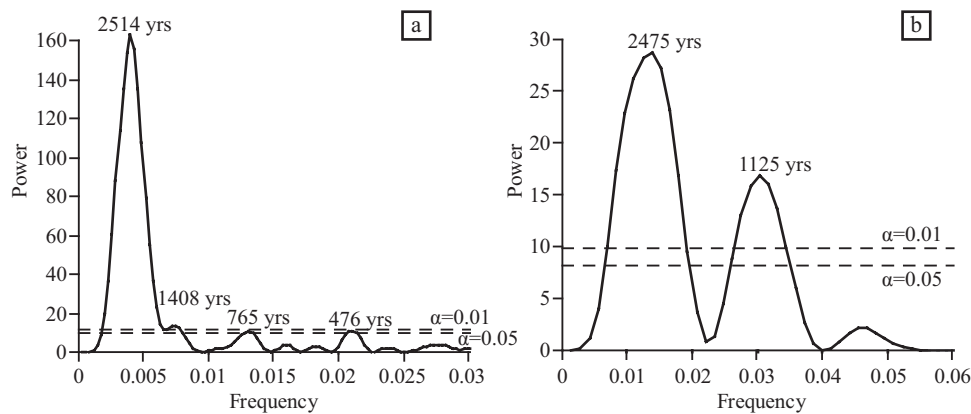
Figure 7. Spectral analysis of (a) $\delta^{13}C$ of Core UV1 (this study) and (b) ^{10}Be of GISP2 ice core (Alley et al., 1995; Davis et al., 1990; Finkel and Nishiizumi, 1997). Exponentially smoothed $\delta^{13}C$ and ^{10}Be data have been de-trended prior to spectral analysis using the PAST program (Hammer et al., 2001). Dashlines show significance levels of 99% (δ=0.01) and 95% (δ=0.05), respectively

The general decrease in C/N ratios up core (Figure 5) also supports the interpretation of weakening monsoon strength. Lower C/N ratios suggest increased proportion of estuarine/ marine particulate organic matter and algae which typically have C/N values < 10 compared with terrestrial organic matter with typical C/N values > 10 (Yu et al., 2010). This suggests reduced terrestrial/freshwater material input due to reduced freshwater flux, hence reduced monsoon precipitation.

General weakening freshwater flux suggested by $\delta^{13}C$ and C/N is supported by the grain size results of core UV1. Modern samples from the Pearl River estuary collected by Yu et al. (2010) suggest that sediments from the riverine area are usually composed of >30% sand and <50% silt, and 17−18% clay, and those from brackish/marine areas usually have >60% silt, <20% sand, and 25−28% clay composition. Domination of clay and silt in the sediment suggests a relatively weak hydrological system under marine/ brackish-water environment at this site during 6600−2200 cal. yr BP. Increase in silt concentrations from generally < 63.6% before ~4600 cal. yr BP, to > 63.6% after ~4400 cal. yr BP, possibly indicates a strengthening marine influence at this site (Figure 5), e.g. changing from brackish to marine conditions responding to reduced freshwater flux. This is supported by the generally increasing clay concentration during 6600–2200 cal. yr BP.

Diatom flora from core UV1 (Figure 6b) show a general increase in marine species since 6650 cal. yr BP. This is interpreted as indicating weakening monsoon-induced freshwater discharge (Zong et al., 2010b). Wang et al. (2005) examined the $\delta^{18}O$ of stalagmites from the Dongge Cave in southern China, and revealed a general decreasing summer monsoon during the past 9000 years (Figure 6c). Pollen records from Jiangxi province, southern China, investigated by Xiao et al. (1998), also show a clear decrease of evergreen trees that prefer humid conditions and shrubs, replaced by herb and ferns in the area, indicating decreasing monsoonal precipitation since early Holocene.

Dry/wet fluctuations at millennial to centennial timescales. Superimposed on the general weakening trend discussed above are centennial- and millennial-scale fluctuations in $\delta^{13}C$ interpreted as wet/dry fluctuations linked to EAM variability during the mid Holocene (shown by the de-trended $\delta^{13}C$ record of Figure 6e). The $\delta^{13}C$ data show one oscillation between 6650 and 4650 cal. yr BP and another oscillation from 4650 to 2150 cal. yr BP (Figure 6e). This suggests a possible periodicity for the EAM precipitation change of around 2000 years. Shorter period, centennial scale, dry events are also suggested by the $\delta^{13}C$ record, for example at 6300, 5700, 4300, 3800, 3400 and 2500 cal. yr BP (shown by horizontal bars in Figure 6e). Each of these dry events lasts for 100−300 years. Spectral analysis on de-trended $\delta^{13}C$ data also suggests two

very significant periodicities of 2514 years and 1408 years (significance level > 99%), and two significant ones of 765 years and 476 years (significance level > 95%; Figure 7a).

Various studies have suggested a general weakening trend in monsoonal climate during the Holocene (e.g. reducing precipitation since the early Holocene), with fluctuations revealed by a range of proxies such as the Loess deposit in central China (e.g. An, 2000) and the stalagmite record from Dongge Cave, southern China (Wang et al., 2005). Zong et al. (2006) examined the bulk organic $\delta^{13}C$ record from the Pearl River estuary and suggested a strong freshwater flux during 8000–6000 cal. yr BP induced by a strong summer monsoon. They then identified a gradual reduction in monsoonal freshwater discharge from 6000 cal. yr BP, with fluctuations towards the present (Zong et al., 2006). Although the high-resolution $\delta^{18}O$ of stalagmite from Dongge Cave (Wang et al., 2005) also indicates the general weakening monsoon since the mid Holocene (Figure 6c), it does not pick up centennial and millennial fluctuations found in $\delta^{13}C$ signal from the Pearl River estuary (Figure 6e and h). This is probably because the $\delta^{18}O$ of stalagmite can be influenced by both temperature and precipitation, and $\delta^{18}O$ of the stalagmite is thought to mainly reflect more local environmental changes (e.g. Kelly et al., 2006) while $\delta^{13}C$ likely shows broader catchment area change.

Driving mechanisms for the EAM variability during the mid Holocene

Orbital forcing. Orbital forcing, specifically the precession cycle, has been suggested as the most important driving mechanism for EAM precipitation variability during the Holocene (An, 2000; An and Thompson, 1998; Huang et al., 2008; Kutzback, 1981; Mayewski et al., 2004). This study shows a general weakening precipitation during the mid Holocene following part of the precession cycle (Figure 6a and d). Precession influences the monsoon through its impact on seasonal contrasts. Half a precession cycle in the past (at approximately the beginning of the Holocene), perihelion occurred in the boreal summer, causing enhanced summer insolation in the Northern Hemisphere, and aphelion fell in the boreal winter, causing reduced winter insolation. Such seasonal contrast was strongest at the beginning of the Holocene and has weakened towards present during the current precession cycle (Figure 6d; Berger and Loutre, 1991; Bradley, 2003). Today, in its slightly elliptical orbit, the Earth is at perihelion around the boreal winter solstice, and at aphelion around the boreal summer solstice (Bradley, 2003). Berger and Loutre (1991) calculated the insolation values at different latitude zones in both summer and winter, showing weakening summer insolation at 30°N (Figure 6d). The weakening East Asian summer monsoon during the 6650−2150

cal. yr BP identified here is most likely a response to the orbital-induced weakening insolation since about 11 000 years BP (An, 2000; Wang et al., 2005).

There are many possible ways that insolation could influence the EAM system. One possible process is that reducing insolation leads to changes in oceanic and atmospheric circulation, resulting in changes in temperature and precipitation (An and Thompson, 1998; Huang et al., 2008; Xiao et al., 2006). For example, reducing insolation results in cooler tropical temperature and thus resulted in a weakened Hadley circulation (Rind and Overpeck, 1993) and reduced water vapour content of the atmosphere. Thereby it would reduce the monsoonal precipitation and resultant freshwater runoff. The influence of precession on the EAM is also supported by a variety of other proxies, e.g. pollen records from the desert/loess transition of north central China (e.g. Jiang et al., 2006) and loess deposits from central China (An et al., 2000; Kukla et al., 1990). Owing to the short record from UV1, this study only demonstrates EAM changes following part of the precession cycle during the mid Holocene.

Solar modulation. Solar activity is one of the possible controlling factors for EAM changes at the millennial timescale. One proxy used to reflect solar modulation (cosmic ray flux) is ^{10}Be concentration in ice cores (Masarik and Beer, 1999; Raisbeck et al., 1990). Studies show that high ^{10}Be concentrations can be attributed to lower solar shielding and consequently to a lower solar activity (Finkel and Nishiizumi, 1997; Muscheler et al., 2004). Horiuchi et al. (2008) analysed an ice core at the Dome Fuji station, inland Antarctica, and found that both the concentration and the flux of ^{10}Be increased at the known solar-activity minimums during the past millennia, e.g. Oort (1010−1050 yr CE) and Wolf (1280−1340 yr CE). Finkel and Nishiizumi (1997) suggest that oscillations in the ^{10}Be concentration of the GISP2 ice core indicate changes in cosmic ray flux and thus (activity of) solar output, as production rates at geomagnetic latitudes above 60° are almost completely insensitive to changes in geomagnetic field intensity (Lal and Peters, 1967). Spectral analysis on ^{10}Be (GISP2 ice core) indicates two significant periodicities of 2475 years and 1125 years (significance level > 99%; Figure 7b), which is similar to the two periodicities (2514 and 1408 years) derived from δ^{13}C (Figure 7a). The similar periodicities at millennial scale, together with a good correlation between de-trended δ^{13}C signal (core UV1) and de-trended ^{10}Be concentration (GISP2, Finkel and Nishiizumi, 1997) (Figure 6e and f) indicate that solar irradiation might be a driving mechanism of EAM variability at millennial and centennial timescales (e.g. Chen et al., 2008).

Although studies have hypothesized several possible correlations between solar activity and the Earth's climate, the exact process controlling how the EAM responds to insolation change still remains unclear. Haigh (1996) suggested that strong solar output increases UV radiation, resulting in an increase in stratospheric O_3. The stratospheric O_3 absorbs radiation and heats up the stratosphere, and the heat propagates down into the troposphere. However, whether the stratospheric heat is strong enough to pass down through the atmosphere far below still needs further investigation. Carslaw et al. (2002) proposed the 'cosmic ray-cloud effect' to explain the link between solar activity and atmospheric processes. Cosmic rays are charged particles with very high energy. Charged particles can move freely along with the magnetic field lines, but not when its track is transverse to the field lines. On their way to the Earth, cosmic rays must cross through interplanetary (IP) magnetic fields, and thus, the stronger IP magnetic field will result in less cosmic rays arriving at the Earth. The strength of the IP magnetic field at solar maxima is almost 1.5 times that at solar minima (Yuming Wang and Tengfei Zhang, personal communication, 2011). Therefore, stronger solar activity will result in fewer cosmic

rays reaching the Earth, which is then correlated with a reduction in cloud cover (Parker, 1958). One possible mechanism for the cosmic ray-cloud effect is suggested by Yu and Turco (2001). Cosmic rays, with their high energy, are able to ionize the atmospheric molecules during the collision, which results in charged molecular clusters. These clusters then work as the condensation nuclei for the cloud formation. Thus shortage of cosmic rays during periods of strong solar activity will discourage cloud formation, and result in higher solar radiation reaching the Earth, resulting in higher Earth surface temperature (Carslaw et al., 2002). As a high ^{10}Be concentration has been found to be related to periods of low solar activity during past millennia at centennial timescales (e.g. Finkel and Nishiizumi, 1997; Horiuchi et al., 2008; Muscheler et al., 2004), the Earth surface temperature would be low during periods of low solar activity indicated by high concentration of ^{10}Be in the GISP2 ice core (Figure 6e; Finkel and Nishiizumi, 1997). Thus, it is possible that at the millennial timescale, solar activity might influence the EAM through changing the Earth surface temperature, and resultant changes in strength of the Siberian High. The Siberian High becomes strong during periods of low solar activity, resulting in strong winter monsoons of low precipitation (e.g. An, 2000). For example, dry and wet periods indicated by de-trended δ^{13}C signal (Figure 6e) are coherent with low and high solar activity indicated by ^{10}Be concentration (Figure 6f).

Solar forcing seems to explain most of the fluctuations observed in this study, however, correlation between EAM and insolation breaks down from 4500 cal. yr BP to 3500 cal. yr BP. Strengthened solar activity around 3930 cal. yr BP indicated by low ^{10}Be concentration (Figure 6f), might result in the wet event around 3990 cal. yr BP indicated by high δ^{13}C (Figure 6e). Solar activity the weakens gradually until *c.* 3300 cal. yr BP (indicated by increasing ^{10}Be concentration, Figure 6f), and correspondingly, the EAM weakens generally.

Other forcing. Decadal to centennial fluctuations in EAM might be due to other forcing, such as high-latitude IRD events (Figure 6g and h). Changes in solar activity have been suggested as a possible forcing mechanism for millennial-scale cooling events in the Northern Atlantic area, such as the North Atlantic ice-rafted debris (IRD) events (Bond et al., 2001). Such correlation is supported by comparison of de-trended ^{10}Be (Figure 6f) and de-trended hematite-stained grain concentration (HSG, Bond et al., 2001) in the North Atlantic sediments (Figure 6g). These changes in the North Atlantic lead to enhanced strength of the Siberian High (Bianchi and McCave, 1999; Rohling et al., 2002) which, in turn, can lead to reduced EAM precipitation. Connection between the IRD events and the EAM is supported by good consistence between de-trended HSG (Figure 6g, Bond et al., 2001) and de-trended δ^{13}C (Figure 6e). For example, three key IRD events from the North Atlantic during the mid Holocene, at 5900−5800, 4300−4100 and 2800−2700 cal. yr BP (Bond et al., 1997; black bars numbered 2, 3 and 4 in Figure 6g) appear to correlate with dry events observed in the Pearl River area, at around 5700, 4300 and 2700 cal. yr BP (black bars in Figure 6e). Dry events observed in UV1 are slightly delayed compared to IRD events suggested by Bond et al (2001). This might be due to the time lag between vegetation change and climate change (likely to be 100–200 years), and the UV1 record is based on vegetation signal.

However, in addition to the dry events addressed above (black bars in Figure 6e), there are other dry events lasting 100−300 years suggested by δ^{13}C (grey bars in Figure 6e). These additional dry events seem to be consistent with low solar activity (Figure 6f), while none of them is correlated with IRD events. These additional dry events might be linked to some regional forcing such as ENSO and possibly high-frequency and low-amplitude changes in the sea level.

Correlation between high-latitude cooling events and the EAM at centennial timescales is supported by the $\delta^{18}O$ record from stalagmites (Figure 6h, Wang et al., 2005). Wang et al. (2005) suggested good correlation between EAM and IRD events during the Holocene, suggesting a possible connection between EAM and high-latitude cooling events. However, comparison between the Pearl River estuary $\delta^{13}C$ record, and the $\delta^{18}O$ from the Dongge Cave, reveals some obvious mismatches. The $\delta^{13}C$ from UV1 indicates two significant dry periods around 5700 and 3500 cal. yr BP, respectively (Figure 6a), while $\delta^{18}O$ from Dongge Cave does seem to suggest a cool period around 5700 cal. yr BP and no obvious change around 3500 cal. yr BP (Figure 6c). It is particularly noticeable that the correlation between our Pearl River estuary record (Figure 6e) and the Dongge Cave stalagmite record (Figure 6h) at a millennial timescale seems to be weak compared with the correlation between the Pearl River estuary, ^{10}Be concentration and HSG records (Figure 6e, f and g). Comparison between $\delta^{13}C$ and ^{10}Be suggests the two dry periods (~5700 and ~3500 cal. yr BP) might be due to low solar activity (Figure 6e and f), while the $\delta^{18}O$ stalagmite record might be more sensitive to local scale variability and thus does not catch up these changes (Figure 6h).

Conclusion

Results from this study suggests that the East Asian Monsoon experienced a general weakening between 6650 and 2150 cal. yr BP. Superimposed on this trend are wet/dry oscillations at millennial to centennial timescales, with major millennial periodicities of about 2500 years and 1400 years, and centennial periodicities of 770 years and 480 years. Our data support the view that orbital-induced precession forcing is the primary controlling mechanism for the monsoonal variability during the Holocene, while solar modulation is a significant forcing for wet/dry oscillations at millennial timescales. Solar activity influences the EAM by changing the strength of Siberian High at millennial timescales (also influencing the North Atlantic through IRD events). Results of this study are supported by other records, especially the high-resolution stalagmite record from Dongge Cave (Wang et al., 2005). However, mismatches between millennial cycles from the $\delta^{13}C$ record presented here and the Dongge Cave $\delta^{18}O$ stalagmite record suggest the Dongge Cave might reflect more local conditions, while $\delta^{13}C$ presented here reflects broader climate conditions.

References

Aitchison JC, Ali JR and Davies AM (2007) When and where did India and Asia collide? *Journal of Geophysical Research, Solid Earth* 112: B05423, doi: 05410.01029/02006JB004706.

Alley RB, Finkel RC, Nishiizumi K, Anandakrishnan A, Shuman CA, Mershon GR et al. (1995) Changes in continental and sea-salt atmospheric loadings in central Greenland during the most recent deglaciation: Model-based estimates. *Journal of Glaciology* 41: 503–514.

An Z (2000) The history and variability of the East Asian paleomonsoon climate. *Quaternary Science Reviews* 19: 171–187.

An Z and Thompson LG (1998) Plaeoclimatic change of monsoonal China linked to global change. In: Galloway J and Melillo J (eds) *Asian Change in the Context of Global Climate Change*. Cambridge University Press, 18–41.

An Z, Porter SC, Kutzbach JE, Xihao W, Suming W, Xiaodong L et al. (2000) Asynchronous Holocene optimum of the East Asian monsoon. *Quaternary Science Reviews* 19(8): 743–762.

Berger A and Loutre M (1991) Insolation values for the climate of the last 10 million years. *Quaternary Science Review* 10(4): 297–317.

Bianchi GG and McCave IN (1999) Holocene periodicity in North Atlantic climate and deep-ocean flow south of Iceland. *Nature* 397(6719): 515–517.

Bird MI, Chivas AR, Radnell CJ and Burton HR (1991) Sedimentological and stable-isotope evolution of lakes in the Vestfold Hills, Antarctica. *Palaeogeography, Palaeoclimatology, Palaeoecology* 84: 109–130.

Bond G, Kromer B, Beer J, Muscheler R, Evans MN, Showers W et al. (2001) Persistent solar influence on North Atlantic climate during the Holocene. *Science* 294: 2130–2136.

Bond G, Showers W, Cheseby M, Lotti R, Almasi P, deMenocal P et al. (1997) A pervasive millennial-scale cycle in North Atlantic Holocene and Glacial climates. *Science* 278: 1257–1266.

Bradley RS (2003) Climate forcing during the Holocene. *Pages News* 11(283): 18–19.

Carslaw KS, Harrison RG and Kirkby J (2002) Cosmic rays, clouds, and climate. *Science* 298: 1732–1737.

Chen F, Yu Z, Yang M, Ito E, Wang S, Madsen DB, Huang X et al. (2008) Holocene moisture evolution in arid central Asia and its out-of-phase relationship with Asian monsoon history. *Quaternary Science Reviews* 27(3–4): 351–364.

Chivas AR, Garclia A, van der Kaars S, Couapel MJJ, Holt S, Reeves JM et al. (2001) Sea-level and environmental changes since the last interglacial in the Gulf of Carpentaria, Australia: An overview. *Quaternary International* 83–85: 19–46.

Davis JC, Proctor ID, Southon JR, Caffee MW, Heikkinen DW, Roberts ML et al. (1990) LLNL/UC AMS facility and research program. *Nuclear Instruments and Methods in Physics Research Section B* B52: 269–272.

Finkel RC and Nishiizumi K (1997) Beryllium 10 concentrations in the Greenland Ice Sheet Project 2 ice core from 3-40 ka. *Journal of Geophysical Research, Ocean* 102(C12), 26: 699–706.

Haigh JD (1996) The impact of solar variability on climate. *Science* 272(5264): 981–984.

Hammer Ø, Harper DAT and Ryan PD (2001) PAST: Paleontological statistics software package for education and data analysis. *Palaeontologia Electronica* 4(1): 9 pp.

Heegaard E, Birks HJB and Telford RJ (2005) Relationships between calibrated ages and depth in stratigraphical sequences: An estimation procedure by mixed-effect regression. *The Holocene* 15: 612–618.

Horiuchi K, Uchida T, Sakamoto Y, Ohta A, Matsuzaki H, Shibata Y et al. (2008) Ice core record of ^{10}Be over the past millennium from Dome Fuji, Antarctica: A new proxy record of past solar activity and a powerful tool for stratigraphic dating. *Quaternary Geochronology* 3: 253–261.

Hu J, Peng Pa, Jia G, Mai B and Zhang G (2006) Distribution and sources of organic carbon, nitrogen and their isotopes in sediments of the subtropical Pearl River estuary and adjacent shelf, Southern China. *Marine Chemistry* 98: 274–285.

Huang G and Yim WWS (2001) An 8000-year record of typhoons in the northern South China Sea. *PAGES News* 9: 7–8.

Huang J, Wang S, Wen X and Yang B (2008) Progress in studies of the climate of humid period and the impacts of changing precession in early–mid Holocene. *Progress in Natural Science* 18: 1459–1464.

Huang Z, Li P, Zhang Z, Li K and Qiao P (1982) *Zhujiang (Pearl) Delta*. Guangzhou: General Scientific Press (in Chinese).

Jiang W, Guo Z, Sun X, Wu H, Chu G, Yuan B et al. (2006) Reconstruction of climate and vegetation changes of Lake Bayanchagan (Inner Mongolia): Holocene variability of the East Asian monsoon. *Quaternary Research* 65: 411–420.

Kelly MJ, Edwards RL, Cheng H, Yuan D, Cai Y, Zhang M et al. (2006) High resolution characterization of the Asian Monsoon between 146,000 and 99,000 years B.P. from Dongge Cave, China and global correlation of events surrounding Termination II. *Palaeogeography, Palaeoclimatology, Palaeoecology* 236(1–2): 20–38.

Kot SC and Hu SL (1995) Water flows and sediment transport in Pearl River Estuary and waves in South China near Hong Kong. In: Civil Engineering Department HKU (ed.) *Proceedings of a Symposium on the Hydraulics of Hong Kong Waters*. Hong Kong, 13–24.

Kukla G, An Z, Melice JL, Gavin J and Xiao JL (1990) Magnetic susceptibility record of Chinese loess. *Transitions of the Royal Society of Edinburgh: Earth Science* 81: 263–288.

Kutzbach JE (1981) Monsoon climate of the early Holocene: climate experiment with the Earth's orbital parameters for 9000 years ago. *Science* 214: 59–61.

Lal D and Peters B (1967) Cosmic ray produced radioactivity on the Earth. In: Fltigge S (ed.) *Handbuch der Physik*. New York: Springer-Verlag, 551–612.

Lamb AL, Vane CH, Wilson GP, Rees JG and Moss-Hayes VL (2007) Assessing $\delta^{13}C$ and C/N ratios from organic material in archived cores as Holocene sea level and palaeoenvironmental indicators in the Humber Estuary, UK. *Marine Geology* 244: 109–128.

Lamb AL, Wilson GP and Leng MJ (2006) A review of coastal palaeoclimate and relative sea-level reconstructions using $\delta^{13}C$ and C/N ratios in organic material. *Earth-Science Reviews* 75: 29–57.

Li P, Qiao P, Zheng H, Fang G and Huang G (1990) *The Environmental Evolution of the Pearl River Delta in the Last 10,000 Years*. Beijing: China Ocean Press (in Chinese).

Mackie EAV, Lloyd JM, Leng MJ, Bentley CJ and Arrowsmith C (2007) Assessment of $\delta^{13}C$ and C/N ratios in bulk organic matter as palaeosalinity indicators in Holocene and Lateglacial insolation basin sediments, northwest Scotland. *Journal of Quaternary Science* 22(6): 579–591.

Malamud-Roam FP, Lynn Ingram B, Hughes M and Florsheim JL (2006) Holocene paleoclimate records from a large California estuarine system and its watershed region: Linking watershed climate and bay conditions. *Quaternary Science Reviews* 25(13–14): 1570–1598.

Masarik J and Beer J (1999) Simulation of particle fluxes and cosmogenic nuclide production in the Earth's atmosphere. *Journal of Geophysical Research* 104: 12 099–12 111.

Mayewski PA, Rohling EE, Curt Stager J, Karlén W, Maasch KA, David Meeker L et al. (2004) Holocene climate variability. *Quaternary Research* 62(3): 243–255.

Middelburg JJ, Nieuwenhuize J, Lubberts RK and van de Plassche O (1997) Organic carbon isotope systematics of coastal marshes. *Estuarine, Coastal and Shelf Science* 45: 681–687.

Mischke S and Zhang C (2010) Holocene cold events on the Tibetan Plateau. *Global and Planetary Change* 72(3): 155–163.

Müller A and Mathesius U (1999) The palaeoenvironments of coastal lagoons in the southern Baltic Sea, I. The application of sedimentary C_{org}/N ratios as source indicators of organic matter. *Palaeogeography, Palaeoclimatology, Palaeoecology* 145: 1–16.

Muscheler R, Beer J and Vonmoos M (2004) Causes and timing of the 8200 yr BP event inferred from the comparison of the GRIP ^{10}Be and the tree ring $\delta^{14}C$ record. *Quaternary Science Reviews* 23: 2101–2111.

Parker EN (1958) Cosmic ray modulation by solar wind. *Physical Review* 110: 1445–1449.

Parnell AC, Haslett J, Allen JRM, Buck CE and Huntley B (2008) A flexible approach to assessing synchronicity of past events using Bayesian reconstructions of sedimentation history. *Quaternary Science Reviews* 27(19–20): 1872–1885.

Porter SC and An Z (2005) Episodic gullying and paleomonsoon cycles on the Chinese Loess Plateau. *Quaternary Research* 64(2): 234–241.

Raisbeck GM, Yiou F, Jouzel J and Petit JR (1990) ^{10}Be and δ^2H in polar ice cores as a probe of the solar variability's influence on climate. *Philosophical Transactions of the Royal Society of London Series A* 330: 65–72.

Rind D and Overpeck J (1993) Hypothesied causes of decade-to-century-scale climate variability: Climate model results. *Quaternary Science Reviews* 12: 357–374.

Rohling EJ, Mayewski PA, Abu-Zied RH, Casford JSL and Hayes A (2002) Holocene atmosphere–ocean interactions: Records from Greenland and the Aegean Sea. *Climate Dynamics* 18(7): 587–593.

Shen J and Wang Y (2009) Primary analysis main silt sources and temporal and spatial changes. *Pearl River* 2: 39–42.

Shi Y, Kong Z, Wang S, Tang L, Wang F, Yao T et al. (1994) Climates and environments of the Holocene Megathermal Maximum in China. *Science in China (Series B)* 37(4): 481–493.

Smittenberg RH, Pancost RD, Hopmans EC, Paetzel M and Damste JSS (2004) A 400-year record of environmental change in an euxinic fjord as revealed by the sedimentary biomarker record. *Palaeogeography, Palaeoclimatology, Palaeoecology* 202: 331–351.

St-Onge G and Hillaire-Marcel C (2001) Isotopic constraints of sedimentary inputs and organic carbon burial rates in the Saguenay Fjord, Quebec. *Marine Geology* 176: 1–22.

Thompson LG, Moseley-Thompson E, Davis ME, Lin PN, Yao T, Dyurgerov M et al. (1993) Recent warming: Ice core evidence from tropical ice cores with emphasis on central Asia. *Global and Planetary Change* 7(1–3): 145–156.

Thompson LG, Thompson ME, Davis ME, Bolzan JF, Dai J, Yao T et al. (1989) Holocene–late Pleistocene climatic ice core records from the Qinghai-Tibetan Plateau. *Science* 246: 474–477.

Wang S and Fen M (1991) The relationship between lake environmental change and strength of southeast monsoon in Daihai Lake, Inner Mongolia. *Science in China Series B* 21(7): 759–768 (in Chinese with English abstract).

Wang Y, Cheng H, Edwards RL, He Y, Kong X, An Z et al. (2005) The Holocene Asian Monsoon: Links to solar changes and North Atlantic climate. *Science* 308: 854–857.

Webster PJ, Magaña VO, Palmer TN, Shukla J and Tomas RA (1998) Monsoons: Processes, predictability, and the prospects for prediction. *Journal of Geophysical Research* 103(C7): 14 451–14 510.

Westman P and Hedenström A (2002) Environmental changes during isolation processes from the Litorina Sea as reflected by diatoms and geochemical parameters: A case study. *The Holocene* 12: 531–540.

Wilson GP, Lamb AL, Leng MJ, Gonzalez S and Huddart D (2005) $\delta^{13}C$ and C/N as potential coastal palaeoenvironmental indicators in the Mersey Estuary, UK. *Quaternary Science Reviews* 24: 2015–2029.

Wu XD (1992) Dendroclimatic study in China. In: Bradley R and Jones P (eds) *Climate Since AD 1500*. London: Routledge, 432–445.

Wu XD, Lin ZY and Sun L (1988) A preliminary study on the climatic change of Hengduan Moutains area since AD 1600. *Advances in Atmospheric Sciences* 5: 437–443.

Xiao J, Wang J, An Z, Wu X and Zhou W (1998) Evidence for the Younger Dryas event in the eastern part of Nanling region. *Acta Botanica Sinica* 40(11): 1079–1082.

Xiao S, Li A, Liu JP, Chen M, Xie Q, Jiang F et al. (2006) Coherence between solar activity and the East Asian winter monsoon variability in the past 8000 years from Yangtze River-derived mud in the East China Sea. *Palaeogeography, Palaeoclimatology, Palaeoecology* 237(2–4): 293–304.

Xu J, Li Y, Cai F and Chen Q (1985) *The Morphology of the Pearl River Estuary*. Beijing: China Ocean Press.

Yamamuro M (2000) Chemical tracers of sediment organic matter origins in two coastal lagoons. *Journal of Marine Systems* 26: 127–134.

Yang S, Tang M, Yim WWS, Zong Y, Huang G, Switzer AD et al. (2011) Burial of organic carbon in Holocene sediments of the Zhujiang (Pearl River) and Changjiang (Yangtze River) estuaries. *Marine Chemistry* 123(1–4): 1–10.

Yu F and Turco RP (2001) From molecular clusters to nanoparticles: Role of ambient ionization in tropospheric aerosol formation. *Journal of Geophysical Research* 106(D5): 4797–4814.

Yu F, Zong Y, Lloyd JM, Huang G, Leng MJ, Kendrick C et al. (2010) Bulk organic $\delta^{13}C$ and C/N as indicators for sediment sources in the Pearl River delta and estuary, southern China. *Estuarine, Coastal and Shelf Science* 87(4): 618–630.

Zhang S, Lu XX, Higgitt DL, Chen C-TA, Han J and Sun H (2008) Recent changes of water discharge and sediment load in the Zhujiang (Pearl River) Basin, China. *Global and Planetary Change* 60: 365–380.

Zhou SZ, Chen FH, Pan BT, Cao JX, Li JJ and Derbyshire E (1991) Environmental change during the Holocene in western China on a millennial timescale. *The Holocene* 1(2): 151–156.

Zong Y (2004) Mid-Holocene sea-level highstand along the southeast coast of China. *Quaternary International* 117: 55–67.

Zong Y, Huang G, Switzer AD, Yu F and Yim WW-S (2009a) An evolutionary model for the Holocene formation of the Pearl River delta, China. *The Holocene* 19(1): 129–142.

Zong Y, Kemp AC, Yu F, Lloyd JM, Huang G and Yim WWS (2010a) Diatoms from the Pearl River estuary, China and their suitability as water salinity indicators for coastal environments. *Marine Micropaleontology* 75(1–4): 38–49.

Zong Y, Lloyd JM, Leng MJ, Yim WW-S and Huang G (2006) Reconstruction of Holocene monsoon history from the Pearl River Estuary, southern China, using diatoms and carbon isotope ratios. *The Holocene* 16(2): 251–263.

Zong Y, Yim WWS, Yu F and Huang G (2009b) Late Quaternary environmental changes in the Pearl River mouth region, China. *Quaternary International* 206(1–2): 35–45.

Zong Y, Yu F, Huang G, Lloyd JM and Yim WW-S (2010b) The history of water salinity in the Pearl River estuary, China, during the Late Quaternary. *Earth Surface Processes and Landforms* 35(10): 1221–1233.

Zong Y, Yu F, Huang G, Lloyd JM and Yim WW-S (2010c) Sedimentary evidence of Late Holocene human activity in the Pearl River delta, China. *Earth Surface Processes and Landforms* 35(9): 1095–1102.